ADVANCED FUNCTIONAL MATERIALS
www.afm-journal.de

AlN: An Engineered Thermal Material for 3D Integrated Circuits

Sam Vaziri, Christopher Perez, Isha M. Datye, Heungdong Kwon, Chen-Feng Hsu, Michelle E. Chen, Maliha Noshin, Tung-Ying Lee, Mehdi Asheghi, Wei-Yen Woon, Eric Pop, Kenneth E. Goodson, Szuya S. Liao, and Xinyu Bao*

Aluminum nitride (AlN) is a promising material for thermal management in 3D integrated circuits (ICs) due to its high thermal conductivity. However, achieving high thermal conductivity in AlN thin films grown at low temperatures on amorphous substrates poses significant challenges for back-end-of-line (BEOL) compatibility. This study reports high cross-plane thermal conductivities approaching 90 $Wm^{-1}K^{-1}$ for sub-300 nm-thick AlN films sputter-deposited at low temperatures (<200 °C) on ordinary SiO_2 substrates. The correlations between cross-plane and in-plane thermal conductivity, texture, grain size, oxygen content, Al:N atomic ratio, and thermal boundary conductance of these films are explored. These findings reveal the crucial role of grain orientation alignment in achieving high thermal conductivity and high thermal boundary conductance. A method is introduced to effectively monitor the thermal conductivity of the AlN thin films using X-ray diffraction. This study offers valuable insights that can aid in the implementation of an effective thermal management material in the semiconductor production line.

1. Introduction

The thermal challenges associated with emerging 3D integrated circuits (3D ICs) can severely limit their power density and overall performance.[1–3] The integration of high thermal conductivity electrical insulators as heat spreaders or routers has been suggested as an effective solution for reducing total thermal resistance and lowering hot spot temperatures.[4] However, developing ultrathin thermally conductive films that meet the required thermal, electrical, and mechanical properties while also being back-end-of-line (BEOL) process compatible remains a significant challenge.[5,6] BEOL compatibility includes low processing thermal budget (<400 °C) and the capability to directly grow high-quality materials on a wide variety of substrates. Among the material candidates such as aluminum nitride (AlN), boron nitride (BN), silicon carbide (SiC), and diamond-like carbon, AlN is a promising choice due to its high crystalline bulk thermal conductivity (≈300 $Wm^{-1}K^{-1}$, near room temperature), decent electrical isolation, and potential process compatibility.[7–11] For example, polycrystalline AlN can be deposited at low temperatures, planarized, and patterned using standard semiconductor processes, which is more challenging with materials such as SiC and diamond. However, the thermal conductivity of any such materials is significantly affected by defect density, crystallinity, and thickness.[8,12]

High thermal conductivity polycrystalline AlN films have been typically reported for thick layers (> 1 µm), deposited on crystalline substrates, and films grown mostly at high temperatures (> 400 °C).[8,13–16] In single crystal defect-free AlN, phonons with mean free paths (MFPs) over 0.3 µm contribute to ≈50% of the heat conduction.[8] This limits the theoretical upper limit of sub-300 nm thin AlN thermal conductivity to ≈150 $Wm^{-1}K^{-1}$. However, in practice, the thermal conductivities[17–23] of such thin films deposited at low temperatures (<400 °C) are below 25 $Wm^{-1}K^{-1}$, limited by a few tens of nanometers of transition amorphous and low quality nano-crystalline AlN near its interface with the substrate.[21,24] The randomly oriented small grains and defects in this region introduce many phonon scattering centers that limit the thermal conductivity even to single-digit values.[18–20]

S. Vaziri, I. M. Datye, H. Kwon, M. E. Chen, M. Noshin, X. Bao
Corporate Research
Taiwan Semiconductor Manufacturing Company Ltd
San Jose, CA 95134, USA
E-mail: svaziri@tsmc.com

C. Perez, H. Kwon, M. Asheghi, K. E. Goodson
Department of Mechanical Engineering
Stanford University
Stanford, CA 94305, USA

C.-F. Hsu, T.-Y. Lee
Corporate Research
Taiwan Semiconductor Manufacturing Company Ltd
Hsinchu 30075, Taiwan

M. E. Chen, E. Pop
Department of Materials Science and Engineering
Stanford University
Stanford, CA 94305, USA

W.-Y. Woon, S. S. Liao
Pathfinding
Taiwan Semiconductor Manufacturing Company
Hsinchu 30075, Taiwan

E. Pop
Department of Electrical Engineering
Stanford University
Stanford, CA 94305, USA

The ORCID identification number(s) for the author(s) of this article can be found under https://doi.org/10.1002/adfm.202402662

DOI: 10.1002/adfm.202402662

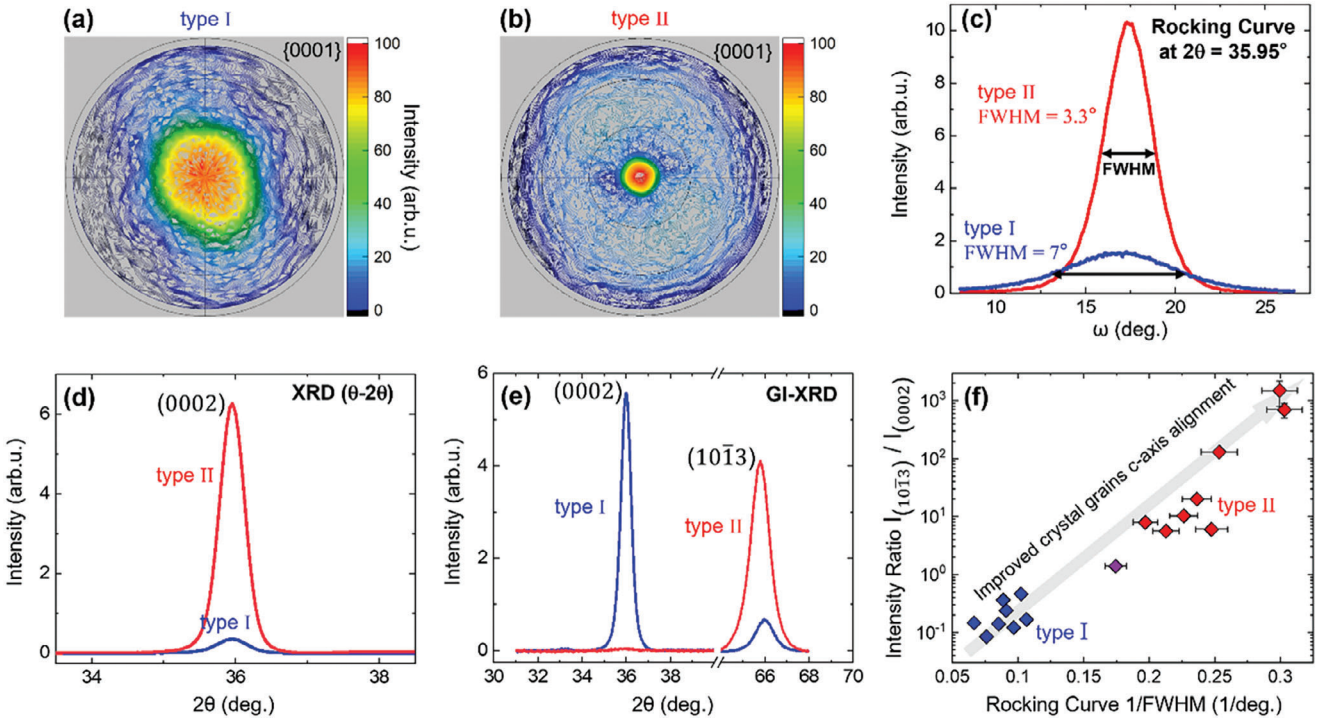

Figure 1. XRD characterization of AlN thin films. (0002) x-ray pole figure for representative a) type I and b) type II AlN thin films. The type II film shows highly c-axis oriented characteristics. c) Rocking curves of the two types of AlN films at $2\theta = 35.95°$, and the corresponding FWHM of the ω-scans. d) XRD $\theta-2\theta$ scans for the representative type I and II films with similar thicknesses. e) GI-XRD for (0002) and (10$\bar{1}$3) peaks of the same samples as in (d). f) The GI-XRD intensity ratio between (10$\bar{1}$3) and (0002) peaks for type I (blue) and type II (red) samples. The purple diamond symbol, which exhibits a close-to-1 $I_{(10\bar{1}3)}/I_{(0002)}$ ratio, is situated in the transitional zone between the two categories of AlN thin films.

In this work, sub-300 nm thin AlN films were deposited by physical vapor deposition (PVD) at low temperature (<200 °C) on thermally-grown amorphous SiO_2 on Si substrates. To establish material development guidelines, the correlation between thermal conductivity and the structural and compositional properties of AlN films were studied. It is revealed that, in addition to grain size and defects, grain orientation alignment or texture can significantly affect both cross-plane and in-plane thermal conductivities of AlN thin films. Highly c-axis textured ultrathin AlN films show cross-plane thermal conductivities approaching 90 $Wm^{-1}K^{-1}$ and AlN/SiO_2 thermal boundary conductance (TBC) approaching 300 $MWm^{-2}K^{-1}$ at room temperature. Thermal anisotropy in such thin films can be up to ≈8X as the c-axis grain orientation alignment improves. Moreover, it is demonstrated that an Al:N atomic ratio <1 can make the film less susceptible to oxidation and improve its thermal conductivity. Finally, grazing incidence angle X-ray diffraction (GI-XRD) is identified as an effective in-line metrology approach to monitor the thermal properties of AlN films.

2. AlN Thin Film Development and Results

2.1. Film Deposition

The AlN thin films were deposited using reactive DC magnetron sputtering of Al with mixed Ar and N_2 plasma as reported in prior works.[25,26] All the AlN thin films were deposited on 14 nm-thick amorphous SiO_2 on Si substrates to be compatible with 3D ICs. AlN films with different structural and compositional properties were grown by modifying the sputtering parameters[27–29] such as pressure, gas composition ($N_2/(Ar+N_2)$: 30% to 98%), DC power (50 to 200 W) and relative position of target and substrate.[30,31] The structural, compositional, and thermal properties of AlN thin films were comprehensively characterized and used to optimize the deposition process for high thermal conductivity films. The details of the deposition can be found in the Supporting Information. The cross-plane and in-plane thermal conductivities of the AlN thin films were measured using pico-second time domain thermoreflectance (TDTR)[32–34] and a DC electro-thermal technique[35] using suspended structures.

2.2. X-Ray Diffraction (XRD) Analysis

A variety of diffraction measurements was performed on the AlN films using PANalytical X'Pert to evaluate the crystallinity, grain size, and texture of the AlN thin films. The AlN thin films studied in this work exhibit two distinct types of texture: weakly textured (type I) and highly textured (type II) samples. In type I samples, the preferential [0001] crystal grain orientation (c-axis) has poor alignment perpendicular to the substrate, whereas in type II samples, the c-axis of the crystal grains is well-aligned perpendicular to the substrate. The texture difference between these two types is qualitatively illustrated in **Figure 1**a,b, which presents the pole figure plots[36] for (0002) planes of representative type I and II samples, respectively. Figure 1c depicts the

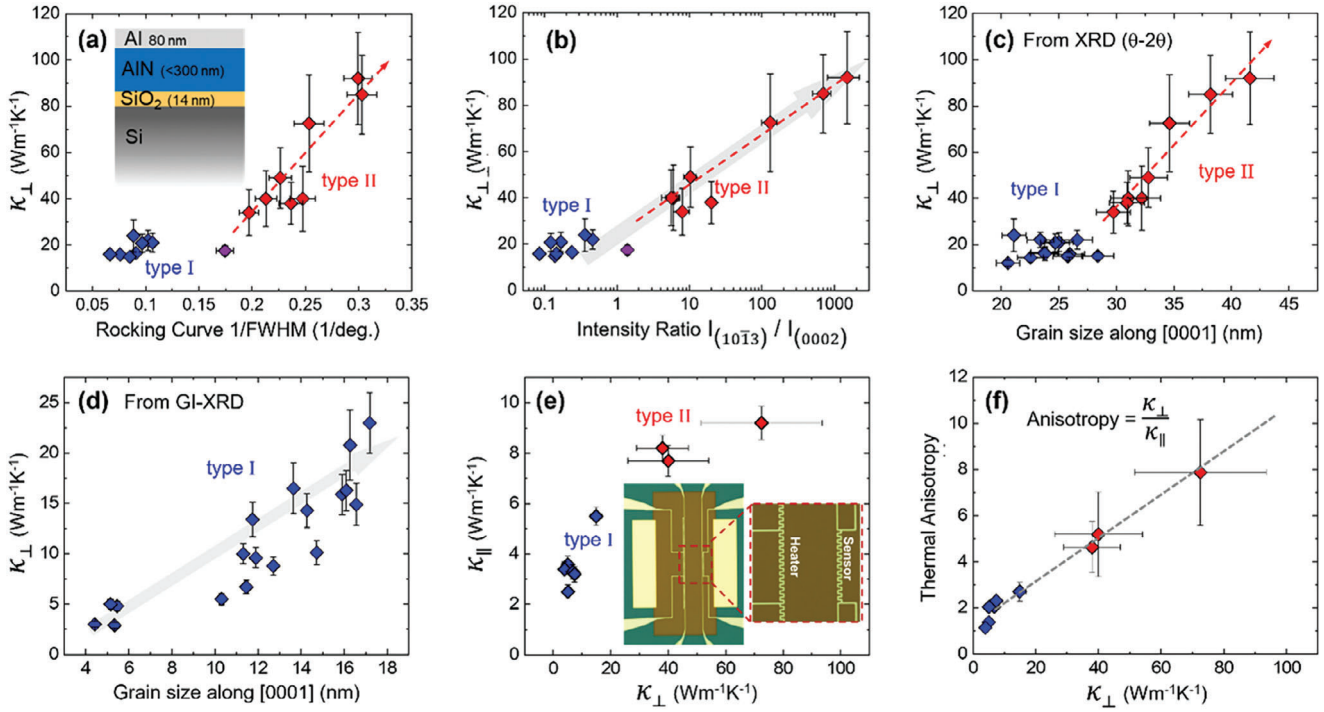

Figure 2. Thermal characterization of AlN thin films. a) Correlation between cross-plane thermal conductivity and 1/FWHM$_\omega$. b) Correlation between cross-plane thermal conductivity and the intensity ratio of $I_{(10\bar{1}3)}/I_{(0002)}$. c) Cross-plane thermal conductivity versus grain size extracted from XRD θ–2θ. d) Cross-plane thermal conductivity versus grain size for type I samples extracted from GI-XRD 2θ scans. e) In-plane thermal conductivity versus cross-plane thermal conductivity. The inset shows a top-view optical image of the structures. f) Thermal anisotropy of AlN films.

rocking curves for (0002) atomic planes, obtained by omega scan ≈18° at a fixed 2θ of 36°. The full width half maximum of the rocking curve (FWHM$_\omega$) is used to quantify the degree of the grain's c-axis alignment along the normal to the sample surface. In this study, the transition point from type I to type II is defined at a FWHM$_\omega$ of 6°, with lower FWHM$_\omega$ implying a higher degree of alignment. Figure 1d shows the (0002) peak in the XRD θ–2θ scans with significantly higher peak intensity for type II than type I samples with similar thicknesses.

Furthermore, GI-XRD in Figure 1e shows two main peaks at ≈36° and 66°, which correspond to (0002) and (10$\bar{1}$3) peaks, respectively. Unlike the θ–2θ scans in Figure 1d,e, shows higher (0002) peak intensity for type I sample and very weak (0002) with dominant (10$\bar{1}$3) peak intensity for type II sample. Due to the small incident angle of GI-XRD (ω = 2°), the Bragg condition is fulfilled only for (0002) planes that are tilted ≈16° with respect to the sample surface.[37,38] Therefore, highly textured type II samples show very weak (0002) GI-XRD peaks. On the other hand, (10$\bar{1}$3) planes in type II samples are favorably oriented to satisfy the Bragg condition in the GI-XRD. Hence, the intensity ratio $I_{(10\bar{1}3)}/I_{(0002)}$ of the GI-XRD peaks can be utilized as a measure of crystal grain alignment. An intensity ratio <1 indicates weakly textured type I samples and >1 indicates well-textured type II samples. Figure 1f shows that the FWHM$_\omega$ and $I_{(10\bar{1}3)}/I_{(0002)}$ of the GI-XRD 2θ scans are well correlated. In the following sections, the thermal conductivity of these two types of samples and their correlation with their structural and compositional characteristics are investigated.

2.3. Cross-Plane Thermal Conductivity

TDTR was used to determine the cross-plane thermal conductivity ($\kappa_\perp$) of the AlN samples and the TBC of the AlN/SiO_2 interface. For such thin films (<300 nm), the TDTR measurement is not sensitive to in-plane thermal conductivity ($\kappa_\parallel$) due to the difference between the in-plane thermal penetration depth and effective beam size.[39] The sensitivity of the TDTR measurement to the cross-plane thermal conductivity and TBC was investigated for a range of parameters that support the samples in this study (see Section S5, Supporting Information). **Figure 2a** shows the correlation between cross-plane thermal conductivity and 1/FWHM$_\omega$ of both types of AlN samples. The measured thermal conductivities of type I samples were <25 $Wm^{-1}K^{-1}$, while type II films exhibit thermal conductivities as high as 92 ± 20 $Wm^{-1}K^{-1}$. This strong correlation was approximately linear for type II samples. In Figure 2b, the cross-plane thermal conductivity also shows a strong correlation with the intensity ratio. The thermal conductivity of type II samples increases from ≈30 to 90 $Wm^{-1}K^{-1}$ within about three orders of magnitude change in the intensity ratio. These results clearly reveal the effect of crystal grain preferential orientation alignment along the heat transfer direction.

In addition to texture, grain size can also significantly affect thermal conductivity due to phonon scattering mechanisms at the grain boundaries.[40] However, the Scherrer model that is widely used for determining grain size from XRD peaks was originally designed for powders with random crystal grain orientation.[41] As a result, it only provides an average estimate

of crystallite size. When applied to randomly oriented grains, the grain sizes obtained from GI-XRD and XRD ($\theta-2\theta$) scans are typically similar. However, in films with some level of texture (grain alignment), the estimations obtained from these two methods may differ. This is because $\theta-2\theta$ scans only probe crystal planes parallel to the sample surface, whereas GIXRD scans examine planes that are tilted with respect to the sample surface. Consequently, the estimated average grain size obtained from this method is also dependent on the alignment of the grain orientation. As a result, the extracted value from Scherrer equation is an *effective* grain size presenting a texture-dependent average grain size.

Figure 2c shows the cross-plane thermal conductivity as a function of average grain size along the [0001] crystal orientation. The grain sizes were calculated from FWHM of (0002) peaks of $\theta-2\theta$ scans using the Scherrer equation. Cross-plane thermal conductivity increases with grain size in type II samples due to the reduced grain boundary density and increased contribution of phonons with longer MFPs. On the other hand, for type I samples, no grain size dependency of thermal conductivity can be observed. This implies that the grains with aligned c-axis perpendicular to the surface and their associated grain boundaries do not significantly affect phonon transport in type I samples. Nevertheless, if the grain sizes are extracted from GI-XRD (0002) peaks, as in Figure 2d, cross-plane thermal conductivity does show a positive correlation with grain size. This originates from the fact that grain sizes calculated from GI-XRD (0002) peaks belong to the grains that are tilted ≈16° with respect to the surface normal. Therefore, misaligned grains dominate the phonon transport in the weakly textured type I samples. (Further discussion is included in Section S2, Supporting Information).

2.4. In-Plane Thermal Conductivity

Thermal anisotropy has a crucial role in heat dissipation in stacked devices, making it an essential parameter for thermal management.[42] The in-plane thermal conductivity of AlN thin films has been less investigated in the past.[14] In this study, a steady-state electrothermal measurement was conducted to study in-plane thermal conductivity for AlN films on suspended SiN membranes in vacuum. The inset in Figure 2e shows a top view optical image of the thermal test structure consisting of a 100 nm-thick SiN free-standing membrane with the Pt central heater and sensor lines. The test structure is capped with 5 nm SiO_2 to promote uniform nucleation. A 3D finite element method model was used to design the membrane aspect ratio and the sensor length to assure the validity of the 1D heat dissipation approximation (see Section S8, Supporting Information). Before AlN deposition, the thermal conductivity of the SiN membrane was measured by forcing current into the central heater line and monitoring the temperature at the pre-calibrated heaters and sensors. Using a 1D analytical thermal model, the in-plane thermal conductivity of the SiN membrane was estimated to be ≈2.5 $Wm^{-1}K^{-1}$ at room temperature, which is in good agreement with previously reported values of SiN films similarly deposited by low-pressure chemical vapor deposition.[43] After the AlN deposition, the measurement was repeated and the in-plane thermal conductivity of the AlN film was extracted. The details of the thermal test structure, models, and measurement are explained in Section S7 (Supporting Information).

Figure 2e shows that the in-plane thermal conductivity of the AlN samples increases from ≈2.5 to >9 $Wm^{-1}K^{-1}$ as the cross-plane thermal conductivity improves. The enhancement of c-axis texture and grain size along [0001] is expected to mainly affect cross-plane thermal conductivity. Plan-view TEM images, shown in Figure S3 (Supporting Information), reveal similar lateral surface grain sizes in both sample types with comparable thicknesses. This suggests that lateral grain size does not significantly contribute to the higher in-plane thermal conductivity observed in type II samples. However, the higher in-plane thermal conductivity in type II samples may have originated from well-ordered vertical grain boundaries that result in small angle boundaries (see Section 2.5 and **Figure 3e**) with lower phonon scattering rates.

The thermal anisotropy ($\kappa_\perp/\kappa_\parallel$) is shown in Figure 2f, which reveals that the anisotropy increases roughly linearly with cross-plane thermal conductivity. This can be understood considering that the grain size and orientation alignment along [0001] are mostly in favor of cross-plane thermal conduction in these columnar structured AlN films. As Figure 2f implies, in the limit of cross-plane thermal conductivity being very small, the thermal anisotropy tends to diminish. This is when the grains are randomly oriented, and the grain sizes become much smaller than the phonon MFP.

2.5. Transmission Electron Microscopy (TEM)

The structural characteristics of the two types of AlN samples were further investigated by TEM analysis. Figure 3a,b shows the representative cross-section low-angle annular dark-field scanning transmission electron microscopy (LAADF-STEM) images of type I and type II AlN thin films, respectively. The TEM imaging tool utilized in this study was manufactured by Thermo Fisher Scientific, specifically the Metrios model, which is equipped with a probe-Cs corrector. To capture STEM images, LAADF mode was employed with a camera length of 295 cm. Both LAADF-STEM images indicate obvious columnar structure of these films. In type I samples in Figure 3a, the grain boundaries are not discernible within a few tens of nanometers of the AlN/SiO_2 interface, implying low quality crystal structures. The columnar structures start to form and the lateral grain size increases with the thickness. However, the columnar structures in type II samples (Figure 3b) begin very close to the interface and extend all the way to the top surface of the film. The high magnification TEM images in Figure 3c–e show examples of the grains' preferential orientation and alignment with the surface normal. Figure 3c shows tilted crystal grains in a type I AlN film. Figure 3d demonstrates well-aligned [0002] orientation along the surface normal and tens of nanometers grain size for a highly textured type II film. Figure 3e shows a high magnification TEM image of the area defined with the blue square in Figure 3d and the corresponding fast Fourier transform (FFT) images. The FFT images reveal the orientation alignment and high crystal quality of the crystal grains. This example further exhibits grain boundaries with small-angle disorientation in the type II sample originating from well-aligned crystal grains. The small-angle boundaries can

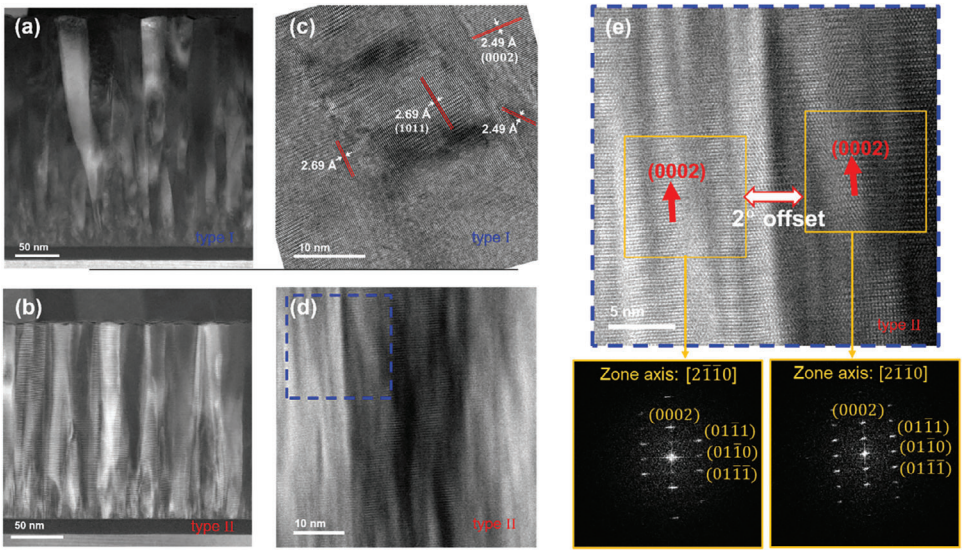

Figure 3. Cross-sectional TEM analysis. The cross-section TEM of representative a) type I and b) type II films show columnar structure characteristics in both sample types. Compared to type II films, type I samples clearly show a poorer crystal quality near the interface with SiO_2 (also observable in Figure 4b,c). c) High magnification cross-sectional TEM of the type I sample shows the tilted c-axis and misaligned grains. The interplanar spacings of 2.49 and 2.69 Å show (0002) and (10$\bar{1}$0) planes, respectively. d) high magnification cross-sectional TEM of type II sample. e) The magnified image of the region shown by blue dashed line in (d), and the FFT of the two adjacent regions.

possibly improve thermal coupling between the grains that explains the higher in-plane thermal conductivity in type II samples. The plan-view TEM images (Figure S3, Supporting Information) further confirm that the lateral grain size at the surface of both types of samples is mostly between 20 and 30 nm.

2.6. Thermal Boundary Conductance (TBC)

As the film thickness decreases and thermal conductivity increases, thermal boundary resistance can significantly contribute to the total thermal resistance.[44] Based on the diffuse mismatch model,[45] the TBC of AlN on Si(111) has been predicted to be ≈150 $MWm^{-2}K^{-1}$. For AlN on amorphous substrates such as SiO_2, the interface coupling and near interface crystal quality of AlN plays an important role in defining the TBC.[22,23] Unlike lattice matched substrates, it is more challenging to promote high crystal quality within the first few nanometers of AlN at the interface, which can significantly limit the TBC. **Figure** 4a shows the TBCs of type I (in blue) and type II (in red) AlN films versus the intensity ratio $I_{(10\bar{1}3)}/I_{(0002)}$. Type I AlN films have TBCs ≈60 to 150 $MWm^{-2}K^{-1}$ that is comparable to the previously reported TBC (100 $MWm^{-2}K^{-1}$) for AlN on amorphous SiN substrate[22] and higher than TBC of AlN on glass (10 $MWm^{-2}K^{-1}$).[23] Figure 4a shows that AlN/SiO_2 interface of type II samples are significantly more conductive with TBCs in the range of 150–300 $MWm^{-2}K^{-1}$.

Figure 4b,c shows cross-sectional TEM images at the AlN/SiO_2 interface and the corresponding magnified images for type I and II samples, respectively. For the type I film, a few nm of an amorphous layer can be observed at the interface. Above this thin amorphous layer, randomly oriented nanometer-size AlN crystallites can be observed. This amorphous layer together with the low-quality poly crystalline AlN near the interface can be the main limiting factors for thermally resistive interfaces in type I films.

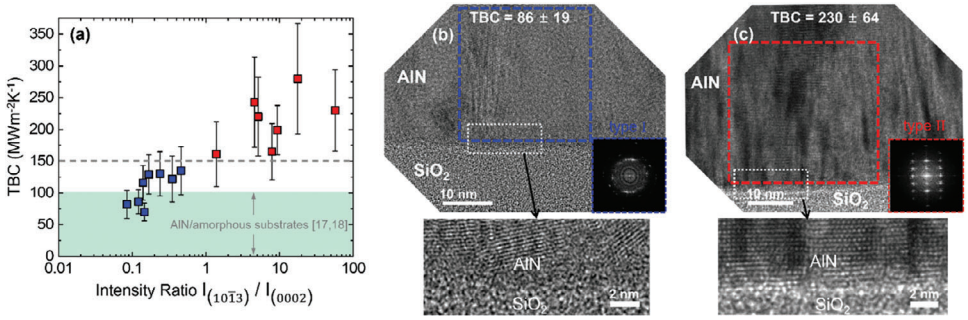

Figure 4. TBC at AlN/SiO_2 interface. a) AlN/SiO_2 thermal boundary conductance of type I and II samples versus intensity ratio $I_{(10\bar{1}3)}/I_{(0002)}$. The TBC shows a positive trend with the c-axis alignment. The shaded area shows the range of previously reported TBC of AlN and amorphous substrate. The dashed line separates the TBC into two regimes for the two types of samples. b,c) cross-sectional TEM images of the AlN on SiO_2 substrate, and the magnified images of the AlN/SiO_2 interface of the area shown by dotted rectangle. The insets show the FFT images of the b) blue, and c) red squares showing lower quality crystalline and interface quality in the type II sample. The TBC values in (b) and (c) are in $MWm^{-2}K^{-1}$.

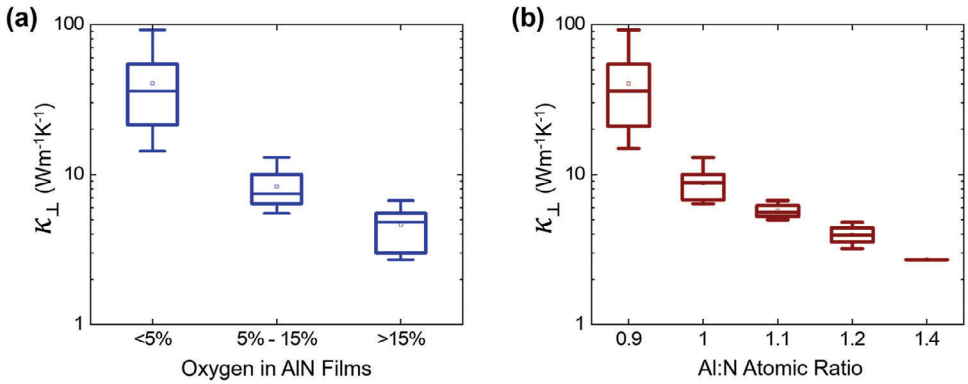

Figure 5. XPS analysis. Cross-plane thermal conductivity of the AlN thin films versus a) oxygen content, in percentage, and b) Al:N atomic ratio. The AlN samples with Al:N atomic ratio between 0.9 and 1, and oxygen content of <5% have the highest thermal conductivities in (a) and (b).

Figure 4c depicts a cross-sectional TEM image of a type II sample, showcasing a sharp and well-defined AlN/SiO_2 interface with (0002) atomic planes grown almost directly on the oxide substrate. This is consistent with the higher TBCs observed in type II samples, as shown in Figure 4a. The well-ordered arrangement of the fine grains at and near the AlN/SiO_2 interface is crucial in achieving thermally conductive boundaries. This finding highlights the significance of optimizing the interfacial microstructure to enhance the thermal performance of the material system. These optimizations can be achieved by controlling the deposition as described in Section S1 (Supporting Information).

2.7. X-Ray Photoelectron Spectroscopy (XPS)

Oxygen is a common impurity that is challenging to avoid in material deposition and processing. In AlN, oxygen replaces N atoms and forms Al—O bonds both at the grain boundaries and also within the AlN film. This process introduces Al vacancies that can significantly reduce the thermal conductivity due to the significant contrast in atomic mass between Al and common impurities (such as Si, O, C, and N atoms).[46–48] The amount of oxygen, in percentage, in the AlN films was estimated using XPS analysis (the details are in the Supporting Information).

Figure 5a shows that the cross-plane thermal conductivity decreases as the oxygen content increases. The oxygen content in type II samples is lower (<5%) compared to type I samples (>5%). This difference can be attributed to the distinct deposition conditions for these two types of samples. The deposition of type II samples occurred at a lower pressure, resulting in reduced oxygen levels in the chamber (see Section S1, Supporting Information). Nonetheless, it is crucial to highlight that texture and grain size remain key factors affecting thermal conductivity in type II samples that show similarly low levels of oxygen. Further analysis of the XPS data, in Figure 5b, reveals a negative correlation between Al:N atomic ratio and cross-plane thermal conductivity. This negative correlation can originate from the higher oxidation susceptibility of Al-rich AlN samples.

3. Thickness Dependency and Benchmark

Figure 6a benchmarks the best thermal conductivity results in this work against previously reported low temperature deposited (<400 °C) AlN films with thicknesses up to 10 µm. The dashed lines in Figure 6a represent an analytical model based on the Boltzmann Transport Equation (BTE) as previously described.[8,16] This model simplifies the contribution of different phonon scattering mechanisms to the dominant effect of point

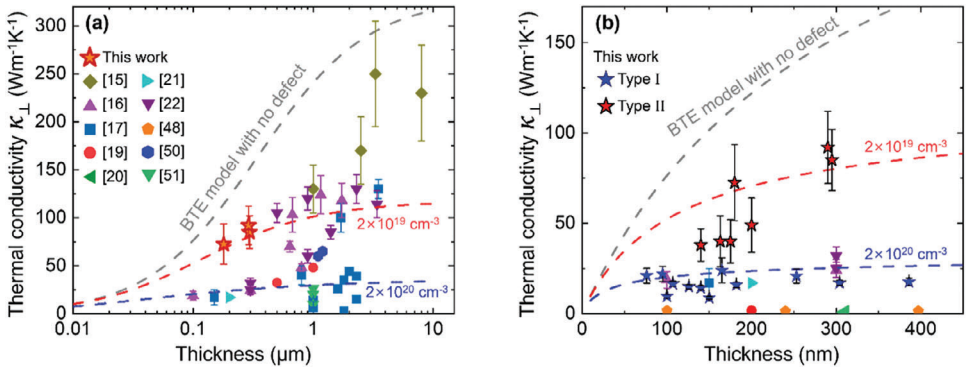

Figure 6. BTE model and benchmark. a) Thermal conductivity versus film thickness, comparing the best results in this work with those from literature deposited at <400 °C.[15–17,19–23,49–52] The dashed lines correspond to BTE predictions for no defect (in gray), 2 × 10^{19} cm^{-3} (in red), and 2 × 10^{20} cm^{-3} (in blue) defect densities. b) Thermal conductivity versus film thickness, comparing type I, type II, and those from literature with thicknesses <400 nm and deposited <500 °C. The type I and type II films show up to one order of magnitude difference in the effective defect density.

defects originating from Al vacancies. This is in line with the experimental results in Figure 5. The dashed lines with different colors show Al defect density modulation. The details of the model are explained in Section S9 (Supporting Information). It is worth noting that this model does not include the effect of texture and grain boundaries but still can be used as an effective comparison. Figure 6b magnifies the region with thicknesses <500 nm that is the focus of this work for high thermal conductivity bonding layer applications. In this figure, more data points are included from both type I and type II AlN films. Type I films show comparable thermal conductivities with literature values, which correspond to films with defect densities $> 2 \times 10^{20}$ cm^{-3}. In type II samples with thermal conductivities approaching 90 $Wm^{-1}K^{-1}$ for 300 nm films, the corresponding defect densities are $<2 \times 10^{19}$ cm^{-3}.

4. Conclusion

Low temperature (<200 °C) AlN film process, structure, composition, and thermal properties are investigated in this work. It is found that besides crystallite size and point defects, the alignment of AlN crystal grains (texture) and structural homogeneity can greatly impact thermal conductivity, thermal boundary conductance, and thermal anisotropy. By incorporating this knowledge and utilizing optimized deposition conditions, it has been possible to achieve remarkably high cross-plane thermal conductivities approaching 90 $Wm^{-1}K^{-1}$ at 300 nm thickness. Well-textured AlN shows thermal anisotropy as high as 8 and a significantly improved thermal boundary conductance at the AlN/SiO_2 interface comparable with the best reported values for AlN on lattice matched substrates. In addition, an alternative approach for monitoring the thermal conductivity and texture of AlN thin films through the utilization of GI-XRD is proposed and verified. This study is an important step toward the inevitable introduction of new materials to the semiconductor production lines. These findings will potentially facilitate the realization and implementation of AlN thin films (sub-300 nm) as a high thermal conductivity bonding layer for thermal management in 3D ICs.

Supporting Information

Supporting Information is available from the Wiley Online Library or from the author.

Acknowledgements

The authors would like to thank Professor H.-S. Philip Wong for his support and insightful feedback, Professor Andrew C Kummel for fruitful discussions, Dr. Arturas Vailionis and Dr. Asir Intisar Khan for their help and support. Part of this work was performed at the Stanford Nano Shared Facilities (SNSF) and nano@stanford, supported by the National Science Foundation under award ECCS-2026822. H.K., M.E.C., and M.N. contributed to this work during internship programs at TSMC Corporate Research.

Conflict of Interest

The authors declare no conflict of interest.

Data Availability Statement

The data that support the findings of this study are available from the corresponding author upon reasonable request.

Keywords

3D IC, aluminum nitride, phonon transport, thermal conductivity, thermal management

Received: February 12, 2024
Revised: May 29, 2024
Published online: June 18, 2024

[1] M. M. Sabry Aly, M. Gao, G. Hills, C.-S. Lee, G. Pitner, M. M. Shulaker, T. F. Wu, M. Asheghi, J. Bokor, F. Franchetti, K. E. Goodson, C. Kozyrakis, I. Markov, K. Olukotun, L. Pileggi, E. Pop, J. Rabaey, C. Ré, H.-S. P. Wong, S. Mitra, *Computer* **2015**, *48*, 24.
[2] M. S. Ebrahimi, G. Hills, M. M. Sabry Aly, M. M. Shulaker, H. Wei, T. F. Wu, S. Mitra, H.-S. P. Wong, in *2014 SOI-3D-Subthreshold Microelectronics Technology Unified Conf. (S3S)*, IEEE, Piscataway, NJ **2014**, pp 1–2.
[3] P. Shukla, A. K. Coskun, V. F. Pavlidis, E. Salman, in *Proc. of the 2019 on Great Lakes Symp. on VLSI*, GLSVLSI '19, Association for Computing Machinery, New York, NY, USA **2019**, pp 439–444.
[4] Ç. Köroğlu, E. Pop, *IEEE Electron Device Lett.* **2023**, *44*, 496.
[5] F. Deprat, C. Fenouillet-Beranger, V. Jousseaume, C. Guerin, V. Beugin, N. Rochat, C. Licitra, V. Caubet-Hilloutou, D. Benoit, G. Imbert, N. Rambal, P. Batude, M. Vinet, *Microelectron. Eng.* **2017**, *167*, 90.
[6] C. Fenouillet-Beranger, S. Beaurepaire, F. Deprat, A. A. de Sousa, L. Brunet, P. Batude, O. Rozeau, F. Andrieu, P. Besombes, M.-P. Samson, B. Previtali, F. Nemouchi, G. Rodriguez, P. Rodriguez, R. Famulok, N. Rambal, V. Balan, Z. Saghi, V. Jousseaume, C. Guerin, F. Ibars, F. Proud, D. Nouguier, D. Ney, V. Delaye, H. Dansas, X. Federspiel, M. Vinet, in *2017 47th European Solid-State Device Research Conf. (ESSDERC)*, IEEE, Piscataway, NJ **2017**, pp 252–255.
[7] G. A. Slack, R. A. Tanzilli, R. O. Pohl, J. W. Vandersande, *J. Phys. Chem. Solids* **1987**, *48*, 641.
[8] R. L. Xu, M. Muñoz Rojo, S. M. Islam, A. Sood, B. Vareskic, A. Katre, N. Mingo, K. E. Goodson, H. G. Xing, D. Jena, E. Pop, *J. Appl. Phys.* **2019**, *126*, 185105.
[9] Z. Cheng, Y. R. Koh, A. Mamun, J. Shi, T. Bai, K. Huynh, L. Yates, Z. Liu, R. Li, E. Lee, M. E. Liao, Y. Wang, H. M. Yu, M. Kushimoto, T. Luo, M. S. Goorsky, P. E. Hopkins, H. Amano, A. Khan, *Phys Rev Mater.* **2020**, *4*, 044602.
[10] W. Li, N. Mingo, *J. Appl. Phys.* **2013**, *114*, 183505.
[11] L. Lindsay, D. A. Broido, T. L. Reinecke, *Phys Rev B* **2013**, *87*, 165201.
[12] Y. Song, C. Zhang, J. S. Lundh, H.-L. Huang, Y. Zheng, Y. Zhang, M. Park, T. Mirabito, R. Beaucejour, C. Chae, N. McIlwaine, G. Esteves, T. E. Beechem, C. Moe, R. Dargis, J. Jones, J. H. Leach, R. M. Lavelle, D. W. Snyder, J.-P. Maria, R. H. Olsson III, J. M. Redwing, A. Ansari, J. Hwang, X. Wang, B. M. Foley, S. E. Trolier-McKinstry, S. Choi, *J. Appl. Phys.* **2022**, *132*, 175108.
[13] Y. R. Koh, Z. Cheng, A. Mamun, M. S. Bin Hoque, Z. Liu, T. Bai, K. Hussain, M. E. Liao, R. Li, J. T. Gaskins, A. Giri, J. Tomko, J. L. Braun, M. Gaevski, E. Lee, L. Yates, M. S. Goorsky, T. Luo, A. Khan, S. Graham, P. E. Hopkins, *ACS Appl. Mater. Interfaces* **2020**, *12*, 29443.
[14] M. S. B. Hoque, Y. R. Koh, J. L. Braun, A. Mamun, Z. Liu, K. Huynh, M. E. Liao, K. Hussain, Z. Cheng, E. R. Hoglund, D. H. Olson, J. A. Tomko, K. Aryana, R. Galib, J. T. Gaskins, M. M. M. Elahi, Z. C.

Leseman, J. M. Howe, T. Luo, S. Graham, M. S. Goorsky, A. Khan, P. E. Hopkins, *ACS Nano* **2021**, *15*, 9588.
[15] K. A. Aissa, N. Semmar, A. Achour, Q. Simon, A. Petit, J. Camus, C. Boulmer-Leborgne, M. A. Djouadi, *J. Phys. Appl. Phys.* **2014**, *47*, 355303.
[16] C. Perez, A. J. McLeod, M. E. Chen, S. Yi, S. Vaziri, R. Hood, S. T. Ueda, X. Bao, M. Asheghi, W. Park, A. A. Talin, S. Kumar, E. Pop, A. C. Kummel, K. E. Goodson, *ACS Nano* **2023**, *17*, 21240.
[17] C. Duquenne, M.-P. Besland, P. Y. Tessier, E. Gautron, Y. Scudeller, D. Averty, *J. Phys. Appl. Phys.* **2011**, *45*, 015301.
[18] Y. Zhao, C. Zhu, S. Wang, J. Z. Tian, D. J. Yang, C. K. Chen, H. Cheng, P. Hing, *J. Appl. Phys.* **2004**, *96*, 4563.
[19] S. R. Choi, D. Kim, S.-H. Choa, S.-H. Lee, J.-K. Kim, *Int. J. Thermophys.* **2006**, *27*, 896.
[20] A. Jacquot, B. Lenoir, A. Dauscher, P. Verardi, F. Craciun, M. Stölzer, M. Gartner, M. Dinescu, *PHOTON-Induc. Surf. Process* **2002**, *186*, 507.
[21] B. E. Belkerk, A. Soussou, M. Carette, M. A. Djouadi, Y. Scudeller, *Appl. Phys. Lett.* **2012**, *101*, 151908.
[22] B. E. Belkerk, S. Bensalem, A. Soussou, M. Carette, H. Al Brithen, M. A. Djouadi, Y. Scudeller, *Appl. Phys. Lett.* **2014**, *105*, 221905.
[23] Y. Bian, M. Liu, G. Ke, Y. Chen, J. DiBattista, E. Chan, Y. Yang, *Sel. Pap. Soc. Vac. Coaters 57th Annu. Tech. Conf.* **2015**, *267*, 65.
[24] J. Jaramillo-Fernandez, J. Ordonez-Miranda, E. Ollier, S. Volz, *Phys. Chem. Chem. Phys.* **2015**, *17*, 8125.
[25] S. T. Ueda, A. McLeod, M. Chen, C. Perez, E. Pop, D. Alvarez, A. C. Kummel, in *2020 Int. Symp. on VLSI Technology, Systems and Applications (VLSI-TSA)*, IEEE, Piscataway, NJ **2020**, pp 110–111.
[26] A. J. McLeod, S. T. Ueda, P. C. Lee, J. Spiegelman, R. Kanjolia, M. Moinpour, J. Woodruff, A. C. Kummel, *Thin Solid Films* **2023**, *768*, 139717.
[27] A. Iqbal, F. Mohd-Yasin, *Sensors* **2018**, *18*, 1797.
[28] K. Umeda, M. Takeuchi, H. Yamada, R. Kubo, Y. Yoshino, *Vacuum* **2006**, *80*, 658.
[29] R. Deng, P. Muralt, D. Gall, *J. Vac. Sci. Technol. A* **2012**, *30*, 051501.
[30] S. Khan, M. Shahid, A. Mahmood, A. Shah, I. Ahmed, M. Mehmood, U. Aziz, Q. Raza, M. Alam, *Prog. Nat. Sci. Mater. Int.* **2015**, *25*, 282.
[31] Y. Chen, R. Wang, B. Wang, T. Xing, X. Song, M. Zhu, H. Yan, *J. Cryst. Growth* **2005**, *283*, 315.
[32] H. Kwon, C. Perez, W. Park, M. Asheghi, K. E. Goodson, *ACS Appl. Mater. Interfaces* **2021**, *13*, 58059.
[33] H. Kwon, C. Perez, H. K. Kim, M. Asheghi, W. Park, K. E. Goodson, *ACS Appl. Mater. Interfaces* **2021**, *13*, 21905.
[34] D. G. Cahill, *MRS Bull.* **2018**, *43*, 782.
[35] C. Dames, *Annu. Rev. Heat Transfer* **2013**, *16*, 7.
[36] J. Fu, *J. Mater. Res. Technol.* **2021**, *14*, 1284.
[37] D. Simeone, G. Baldinozzi, D. Gosset, S. L. Caer, J.-F. Bérar, *Thin Solid Films* **2013**, *530*, 9.
[38] A. Pandey, S. Dalal, S. Dutta, A. Dixit, *J. Mater. Sci. Mater. Electron.* **2021**, *32*, 1341.
[39] C. Perez, A. Jog, H. Kwon, D. Gall, M. Asheghi, S. Kumar, W. Park, K. E. Goodson, *Adv. Funct. Mater.* **2022**, *32*, 2207781.
[40] J. Cho, D. Francis, P. C. Chao, M. Asheghi, K. E. Goodson, *J. Heat Transf.* **2015**, *137*, 071303.
[41] A. L. Patterson, *Phys. Rev.* **1939**, *56*, 978.
[42] W. Y. Woon, S. Vaziri, C. C. Shih, I. Datye, M. Malakoutian, J. Hsu, K. F. Yang, J. R. Huang, T. M. Shen, S. Chowdhury, X. Y. Bao, S. S. Liao, in *Proc. 2023 International Electron Devices Meeting (IEDM)*, IEEE, San Francisco, CA, USA, **2023**, pp. 1–4.
[43] H. Ftouni, C. Blanc, D. Tainoff, A. D. Fefferman, M. Defoort, K. J. Lulla, J. Richard, E. Collin, O. Bourgeois, *Phys. Rev. B* **2015**, *92*, 125439.
[44] S. Vaziri, E. Yalon, M. M. Rojo, S. V. Suryavanshi, H. Zhang, C. J. McClellan, C. S. Bailey, K. K. H. Smithe, A. J. Gabourie, V. Chen, S. Deshmukh, L. Bendersky, A. V. Davydov, E. Pop, *Sci. Adv.* **2019**, *5*, eaax1325.
[45] W. A. Little, in *From High-Temperature Superconductivity to Microminiature Refrigeration*, Eds: B. Cabrera; H. Gutfreund, V. Kresin, Springer, Berlin, Germany **1996**, pp. 15–30.
[46] J. Jarrige, J. P. Lecompte, J. Mullot, G. Müller, *Int. Symp. Nitrides Journees Etudes Sur Nitures* **1997**, *17*, 1891.
[47] R. Kobayashi, Y. Moriya, M. Imamura, K. Oosawa, K. Oh-Ishi, *J. Ceram. Soc. Jpn.* **2011**, *119*, 291.
[48] J. Kim, J.-Y. Kim, H. Ahn, M. H. Jeong, E. Lee, K. Cho, S.-M. Lee, W. Shim, J.-H. Pee, *Materials* **2022**, *15*, 8125.
[49] Y. Zhao, C. Zhu, S. Wang, J. Z. Tian, D. J. Yang, C. K. Chen, H. Cheng, P. Hing, *J. Appl. Phys.* **2004**, *96*, 4563.
[50] J. T. Gaskins, P. E. Hopkins, D. R. Merrill, S. R. Bauers, E. Hadland, D. C. Johnson, D. Koh, J. H. Yum, S. Banerjee, B. J. Nordell, M. M. Paquette, A. N. Caruso, W. A. Lanford, P. Henry, L. Ross, H. Li, L. Li, M. French, A. M. Rudolph, S. W. King, *ECS J. Solid State Sci. Technol.* **2017**, *6*, N189.
[51] B. E. Belkerk, J. Camus, B. Garnier, H. Al Brithen, S. Sahli, M.-A. Djouadi, *Int. J. Therm. Sci.* **2020**, *151*, 106259.
[52] T. S. Pan, Y. Zhang, J. Huang, B. Zeng, D. H. Hong, S. L. Wang, H. Z. Zeng, M. Gao, W. Huang, Y. Lin, *J. Appl. Phys.* **2012**, *112*, 044905.

ADVANCED FUNCTIONAL MATERIALS

Supporting Information

for *Adv. Funct. Mater.*, DOI 10.1002/adfm.202402662

AlN: An Engineered Thermal Material for 3D Integrated Circuits

Sam Vaziri, Christopher Perez, Isha M. Datye, Heungdong Kwon, Chen-Feng Hsu, Michelle E. Chen, Maliha Noshin, Tung-Ying Lee, Mehdi Asheghi, Wei-Yen Woon, Eric Pop, Kenneth E. Goodson, Szuya S. Liao and Xinyu Bao*

Supporting Information for:

AlN: An Engineered Thermal Material for 3D Integrated Circuits

S. Vaziri[1], C. Perez[2], I. M. Datye[1], H. Kwon[1,2], C. F. Hsu[3], M. Chen[1,4], M. Noshin[1], T. Y. Lee[3], M. Asheghi[2], W. Y. Woon[5], E. Pop[4,6], K. E. Goodson[2], S. S. Liao[5], X. Y. Bao[1]

[1]Corporate Research, Taiwan Semiconductor Manufacturing Company Ltd, San Jose, CA, 95134, USA

[2]Department of Mechanical Engineering, Stanford University, Stanford, CA, 94305, USA

[3]Corporate Research, Taiwan Semiconductor Manufacturing Company Ltd, Hsinchu, 30075, Taiwan

[4]Department of Materials Science and Engineering, Stanford University, Stanford, CA, 94305 USA

[5]Pathfinding, Taiwan Semiconductor Manufacturing Company, Hsinchu, 30075, Taiwan

[6]Department of Electrical Engineering, Stanford University, Stanford, CA, 94305, USA

S1. AlN sputter deposition

The AlN films were deposited by DC reactive magnetron sputtering using an AJA ATC 1800-F sputtering system, without active substrate heating or cooling. During the deposition, the substrate temperature increases and saturates, after a while, due to exposure to the plasma and impact of sputtered Al. The substrate temperature increase depends on the deposition condition and the thermal coupling between the substrate and stage. In our experiments, the substrate temperature saturates mostly between 90°C and 130°C.[1] For BEOL integration compatibility, the process should be limited to 400°C.

Two types of substrates were used in this study. For our standard SiO_2/Si substrates, ~14 nm-thick SiO_2 layer was formed on Si(100) substrates using an oxidation process. For in-plane thermal conductivity test structures, ~100 nm-thick LPCVD SiN on Si(100) substrates were utilized. Prior to the sputter deposition,

the substrates were cleaned using acetone and isopropyl alcohol (IPA). Following 5 min Al target pre-sputter cleaning, the deposition was performed at a desired gas composition (N_2/(Ar+N_2): 30% to 98%), pressure (2-8 mTorr), DC power (50-200 W), and target-to-substrate distance (10-30 cm). A total number of about 90 depositions were performed in this study. Type II AlN films with higher thermal conductivity and (0002) grain alignment were achieved at the higher range of gas composition (N_2/(Ar+N_2): 80% to 98%) and DC power (150-200 W), and lower range of pressure (2-3 mTorr) and target-to-substrate distance (10-14 cm). It has been previously shown that (0002) texture can be improved by adjusting target-to-substrate distance, working pressure and DC power.[2,3]

The thicknesses of the films were measured by atomic force microscopy (AFM) and X-ray reflection (XRR) using Park XE-100 and Philips PANalytical X'Pert, respectively. In this study, the AlN thin film thicknesses are mostly between 100 nm and 300 nm. All the substrates were about 2 cm × 2 cm (length × width). The thickness variation across each sample is < 3% and between samples, with same deposition parameters, is < 6%. For the TDTR measurement, an 80 nm-thick Al transducer was deposited on top of the samples using electron beam evaporation (AJA International Inc., ATC-E Series). Three points on each sample were measured by TDTR and the variations were incorporated in the total error of the thermal conductivity. In these samples, the thermal conductivity point to point variation is within the fitting and thickness errors.

S2. X-ray diffraction analysis

A GI-XRD pattern of an AlN sample with weak c-axis texture is shown in Figure S1. To estimate the size of crystallites in sputtered films, the (0002) diffraction peak of the AlN samples was utilized along with the Scherrer equation[4] (1):

$$C.S. = \frac{0.94\lambda}{\beta \cos(\theta)}, \qquad (1)$$

where λ represents the x-ray wavelength, β is the peak FWHM in radians, and θ is the diffraction angle. It should be noted that this equation was originally meant for powders, but the estimated crystallite sizes, also known as grain sizes, are only intended for comparative purposes within our datasets.

We note that the extracted grain sizes from GI-XRD (0002) peak provide an average grain size along [0001] that are tilted roughly 16° with respect to the surface normal. However, if XRD (θ-2θ) pattern is used, the grain sizes correspond mostly to the grains with c-axis roughly aligned with the perpendicular to the substrate. The thermal conductivity of type I and II AlN samples in the cross-plane direction were analyzed in relation to the effective grain size extracted from XRD (θ-2θ) and GI-XRD patterns, as shown in Figure S2a and b. For type I samples, no clear trend was observed in Figure S2a, indicating that vertically aligned [0001] grains did not play a significant role in cross-plane heat transfer. In contrast, Figure S2b demonstrates a positive correlation between thermal conductivity and grain size for type I samples. For type II samples in Figure S2a, a clear positive correlation was observed between thermal conductivity and the effective grain size along [0001]. However, no trend can be observed in Figure S2b, implying that tilted grains do not significantly contribute to the cross-plane heat transfer in type II samples.

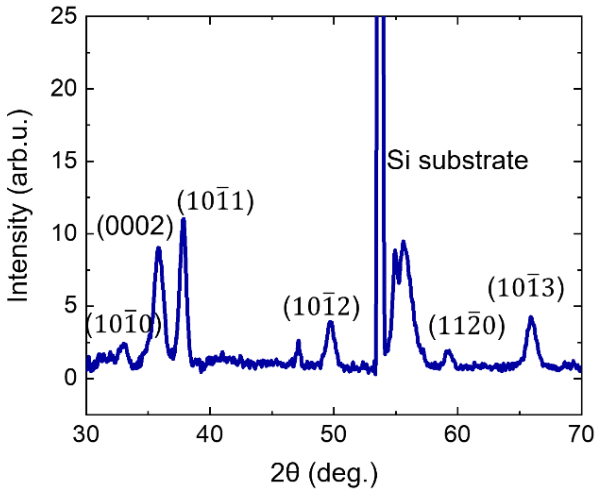

Fig. S1 GI-XRD. GI-XRD scan of a type I sample showing characteristic AlN and Si substrate peaks.

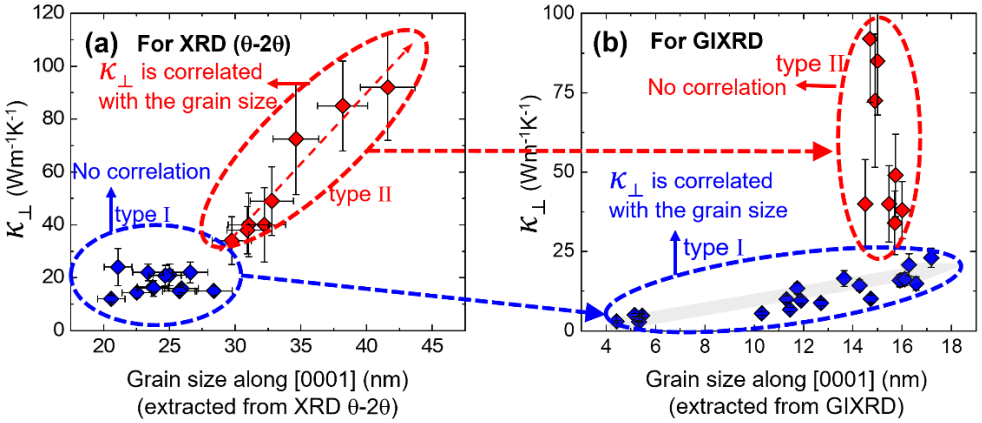

Fig. S2. Thermal conductivity versus grain size along [0001] (a) extracted from XRD, θ-2θ scans, and (b) from GI-XRD scans.

S3. TEM

Figure S3a and b show the plan-view TEM images of type I and type II samples, respectively. The lateral grain size at the surface of both types of samples is mostly between 20 nm and 30 nm. However, the corresponding FFT insets imply more randomly oriented grains in Figure S3a and a weak in-plane preferential orientation for type II samples in Figure S3b. Figure S3c and d show higher magnification images and the corresponding FFTs of multigrain and single grain areas confirming random orientation in type I samples and a higher degree of alignment in type II samples. The dashed lines in Figure S3e and f are guidelines for atomic planes in some of the grains with the corresponding crystal plane distances. The measured 2.67 and 2.69 Å atomic distances are in good agreement with the interplanar distances in (10$\bar{1}$0) planes.

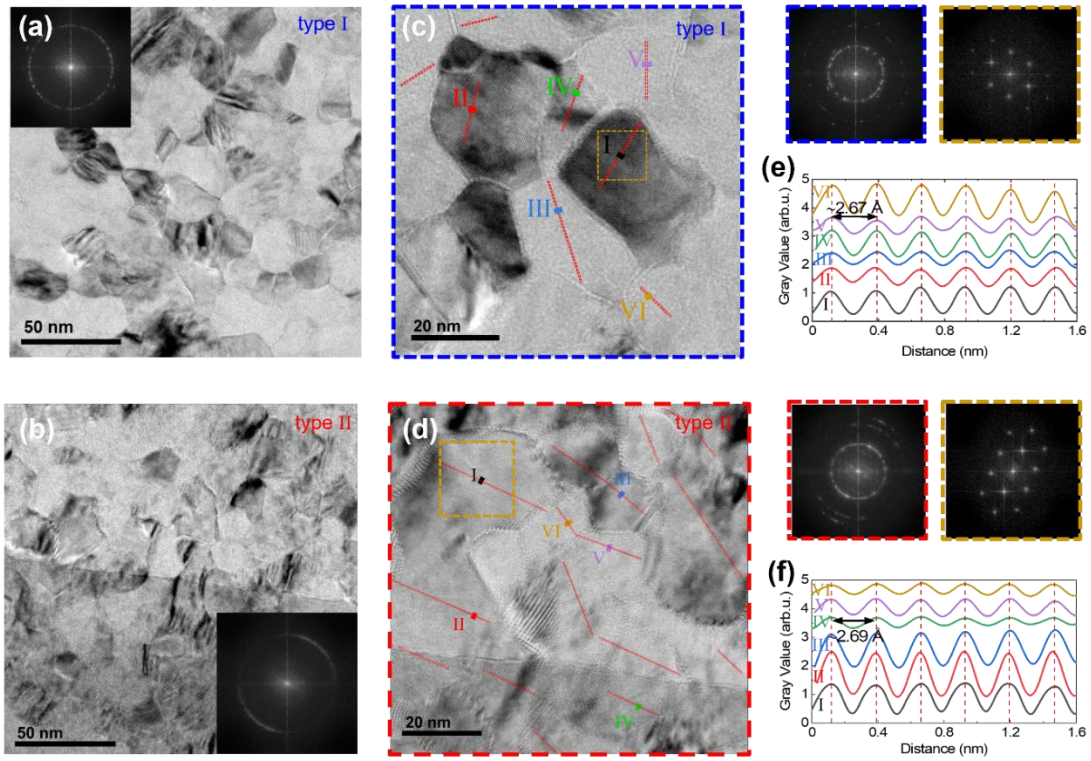

Fig. S3 Plan-view TEM analysis. (a) The plan-view TEM of representative (a) type I and (b) type II films showing the lateral grain size mostly in the range of 20 nm to 30 nm. The insets show the corresponding FFT images. (c) and (d) are high magnification images of (a) and (b). The FFT images correspond to the blue- and orange-dashed squares in (c), and red- and yellow-dashed squares in (d). (e) and (f) are measurements of the interplanar distances in (c) and (d), respectively.

S4. XPS

The XPS measurements were performed using a PHI VersaProbe 3 with an x-ray spot size of 200 µm at a power of 50 W. In order to measure the film composition below the surface, high resolution depth profiles with a pass energy of 140 eV were performed using Ar sputtering (2 kV Ar ions) to etch the film and measure the XPS spectra throughout the depth of the film. The percentage of each element (O, Al, and N) was obtained by taking an average over all the depths measured below the surface. A representative depth profile is shown in Figure S4 for an AlN film with high thermal conductivity. The atomic concentration of each element (including Carbon) is shown as a function of Ar sputter time. After the initial surface measurement (at 0 min), the atomic concentration is relatively stable throughout the thickness of the film.

All the type II samples exhibit an oxygen content of <3% and Al:N atomic ratio of about 0.9, implying that the structural characteristics of the type II samples are the dominant factors defining the thermal properties of these films.

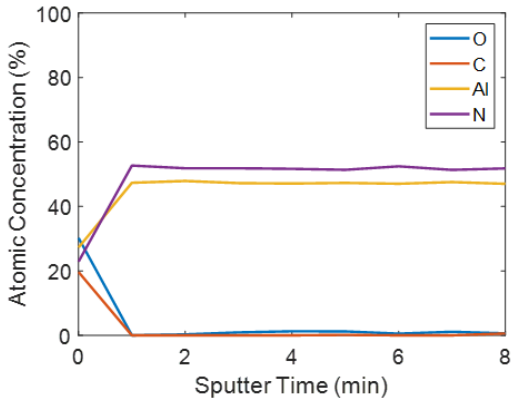

Fig. S4 XPS depth profile. Representative XPS depth profile of an AlN film with high thermal conductivity. The O and C concentrations are relatively high at the surface (0 min sputter time), but they drop (to <1%) below the surface (≥1 min sputter time). The O, Al, and N percentages are obtained by taking an average over the values below the surface (from 1 min to 8 min of sputter time).

S5. Time-domain thermoreflectance (TDTR)

We utilized TDTR to determine the thermal properties of the AlN films, employing the same methodology in previous publications.[1,5] In the TDTR system, a Nd:YVO_4 laser generates a pulsed laser beam at a repetition rate of approximately 82 MHz, with a wavelength of 1064 nm. The optical isolator directs the laser beam through a half-wave plate and a polarizing beam splitter (PBS), dividing it into a pump beam path and a probe beam path. The pulsed laser in the pump beam path is modulated by an electro-optic modulator (EOM) for lock-in detection. Additionally, its wavelength is halved at a second harmonic generator (SHG) to filter it out from the probe pulses. The sample is irradiated with the pump beam after it is reflected by a cold mirror, and the beam is focused onto the sample using a 20X objective lens. The probe beam pulses, after passing through the polarizing beam splitter, undergo temporal delay via a mechanical delay stage. The delayed probe beam pulses then pass through a non-polarized beam splitter, a half-wave plate, and a linear polarizer to adjust the polarization orientation. The probe beam is finally reflected from the sample surface and detected by a photodetector, which is connected to a lock-in amplifier. The resulting in-phase and out-of-phase voltage signals from the lock-in amplifier are then utilized to determine the thermal properties of the sample.[6] Knife-edge measurements were performed to determine the focused radii of the pump and probe beams, with values of 5.36 ± 0.1 and 3.19 ± 0.05 μm, respectively. A pump power of 9.5 mW, modulated at 10 MHz, was used, while the probe was set to 3 mW and focused onto the sample surface using a 20× objective lens. We then fit the thermoreflectance data to a 3D heat diffusion model for a multi-layer stack of materials, using the unknown properties of interest as parameters to converge measurement and theory. The controlled parameters were obtained from either independent measurements or literature data. We also independently determined the thermal conductivity of the Al transducer and substrates using TDTR. The uncertainties resulting from these independent measurements were incorporated into our thermal model to determine the total uncertainty of the measurement.

The sensitivity of an unknown property, x, on the measured TDTR signal is determined by

$$S_x = \frac{\partial \ln(r)}{\partial \ln(x)}, \qquad (2)$$

where r is the ratio ($-V_{in}/V_{out}$) in this study. Figure S5a and b depict the outcomes of the sensitivity analysis carried out on AlN films with thicknesses of 100 nm and 200 nm, respectively, formed on 14 nm-thick SiO_2 on Si substrates. The thermal conductivities were assumed to be 10, 20, 30, 40 and 70 $Wm^{-1}K^{-1}$ for each film thickness.

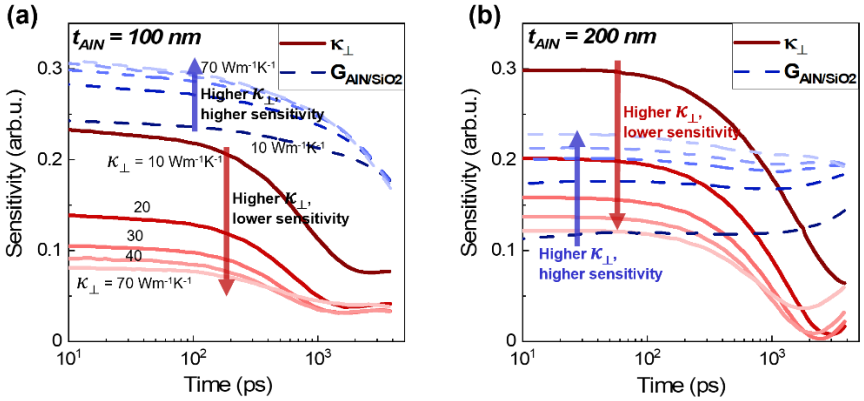

Fig. S5 TDTR signal sensitivity. Sensitivity of cross-plane thermal conductivity ($\kappa_\perp$) and AlN/SiO_2 thermal boundary conductance ($G_{AlN/SiO2}$) to signal ratio for (a) 100 nm-thick and (b) 200 nm-thick AlN films.

S6. Fabrication of the thermal test structures

Figure S6 shows an example of our thermal test structures that were designed and fabricated for in-plane thermal conductivity measurements.[7] Low-pressure chemical vapor deposition was used to grow about 100 nm SiN on Si(100) substrates. Backside SiN was patterned using photolithography and reactive ion etching to open windows to the underneath Si. Through these openings, the Si was etched using KOH to reveal the frontside SiN as suspended membranes. The heater and sensor metal lines were formed by 5/40 nm Cr/Pt electron beam physical vapor deposition and lift-off process. Another metallization and lift-off process was utilized to form 5/70 nm Ti/Au contact pads, metal lines, and local heat sinks to ensure uniform 1D heat transport.

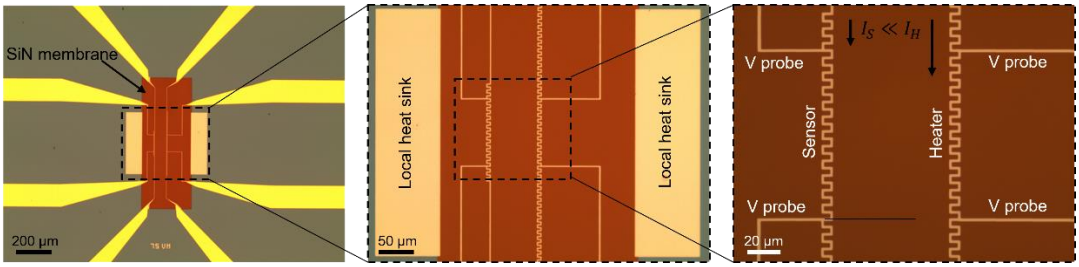

Fig S6. Optical micrograph of a thermal test structure with suspended membrane.

S7. Electrothermal measurement of in-plane thermal conductivity

The thermal test structures are used to measure the in-plane thermal conductivity of the SiN membranes and AlN films.[7,8] Before the AlN deposition, the temperature coefficient of resistance (TCR) for each metal line is measured using a four-probe resistance measurement on a hot plate in vacuum. Next, a current, from 10 µA to 800 µA, is applied to the central heater line. The maximum applied current depends on the structure dimensions and material. Using the voltage probes with 100 µm spacing, the resistance of the center part of the heater line is monitored. A four-probe resistance measurement is simultaneously carried out on the sensor metal line using 10 µA forced current to avoid heating. Using the TCR of the metal lines, the temperature rise in the heater and sensor is defined at any heater current (see Figure S7a). Finally, the thermal conductivity of the SiN membrane can be calculated using a simplified 1D model:

$$\kappa_{\parallel} = \frac{Qd}{2tL(\Delta T)}, \qquad (3)$$

where Q is the electrical input power, d is the distance between heater and sensor, t is the thickness of the SiN membrane (~110 nm), L is the distance between the voltage probe metal lines (100 µm), and ΔT is the temperature difference between the heater and sensor metal lines ($T_H - T_S$). The thermal conductivity of the SiN membrane is determined to be 2.6 ± 0.2 $Wm^{-1}K^{-1}$.

After the AlN deposition, the same procedure is repeated, starting from the TCR measurement. Using equation (2) with t being the total thickness of the SiN and AlN films, the effective thermal conductivity of the stack, and consequently the thermal conductivity of the AlN film, is calculated, as shown in Figure S7b.

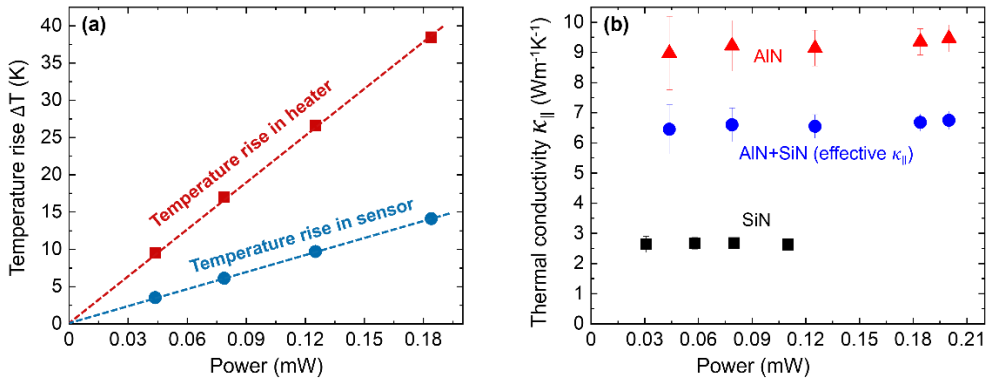

Fig. S7 Electrothermal measurement. (a) Temperature rise in heater and sensor versus electrical power. (b) Extracted thermal conductivity from the electrothermal measurements for SiN, SiN+AlN, and AlN.

S8. FEM simulations

We performed finite element simulations using COMSOL Multiphysics to design the experiment for measurement of in-plane thermal conductivity and to verify the accuracy of the thermal conductivity extraction. To simplify the model, only half of the geometry is simulated by splitting it along the line of symmetry. In Figure S5, the dimensions of the SiN membrane are chosen to be $L_{membrane}$ = 600 µm,

$W_{membrane}$ = 166 µm, and the width of the heater W_{heater} = 1.5 µm. The thickness of the SiN is ~112 nm, and the thickness of the AlN on top of the SiN is 173 nm. The heater to sensor distance is 50 µm, and the current applied to the heater line is 600 µA. These parameters are chosen to ensure sufficient heating at the heater and sensor. A 3D temperature map is included in Figure S8a with the corresponding 2D top-view thermal map in Figure S8b, showing the highest temperature along the heater and reduced temperature along the width of the membrane. The temperature profiles along the membrane at the heater and sensor are shown in Figure S8c, showing good agreement with the experimentally measured temperature at the heater and sensor. These simulations verify the extracted thermal conductivity of the SiN and AlN films and confirm the accuracy of the 1D thermal model.

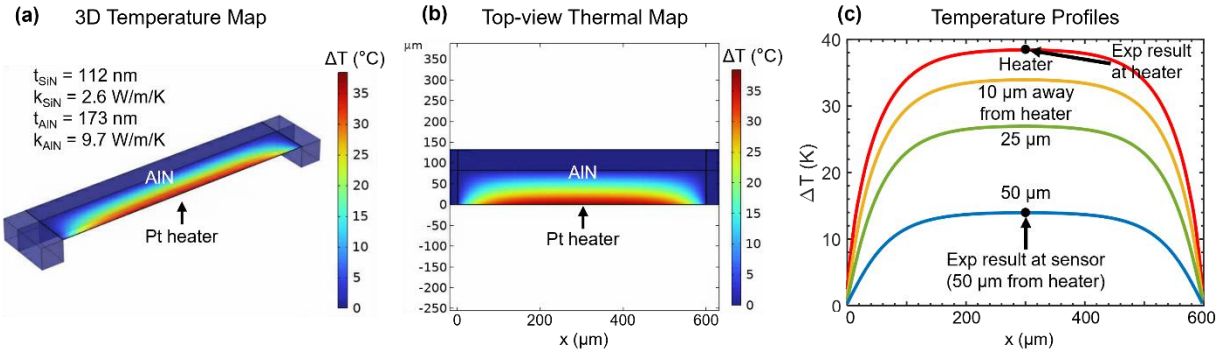

Fig. S8 FEM simulations. (a) 3D temperature map and (b) the corresponding 2D top-view thermal map of a thermal test structure with 600 µA current applied to the heater. The membrane length ($L_{membrane}$), membrane width ($W_{membrane}$), and heater width (W_{heater}) are 600 µm, 166 µm and 1.5 µm, respectively. The thickness of the SiN is ~112 nm, and the thickness of the AlN on top of the SiN is ~173 nm.

S9. Boltzmann Transport Equation predictions

We use a lattice thermal conductivity model based on the Boltzmann transport equation (BTE),[1,9,10] expressed as

$$\kappa_{\perp} = \frac{1}{3} C v \lambda = \frac{1}{3} \sum_{j} \int_{0}^{\omega_{max}} \hbar \omega D(\omega) \frac{\partial f_{BE}^{0}(\omega, T)}{\partial T} v_j^2 \tau_j(\omega) d\omega \,, \qquad (4)$$

where C is the volumetric heat capacity, v is the phonon velocity, λ is the phonon mean free path, ω_{max} is the Debeye cutoff frequency, $D(\omega)$ is the phonon density of states, f_{BE}^{0} is the Bose-Einstein equilibrium function, T is the temperature, and $\tau(\omega)$ is the phonon relaxation time. Using a similar simplification approach as in previous studies, Al vacancies are the point defects with dominant effect on thermal conductivity in AlN. In this study, we use Al defect density in conjunction with the following expression for point defect scattering rate[2,6]

$$\frac{1}{\tau_D} = \frac{V}{4\pi v^3} \omega^4 \sum_{j} f_i \left(\frac{m - m_i}{m}\right)^2, \qquad (5)$$

where f_i represents the fractional concentration of the *i*th impurity atom, and m and m_i denote the masses of the original and *i*th impurity atoms, respectively.

References

(1) Perez, C.; McLeod, A. J.; Chen, M. E.; Yi, S.; Vaziri, S.; Hood, R.; Ueda, S. T.; Bao, X.; Asheghi, M.; Park, W.; Talin, A. A.; Kumar, S.; Pop, E.; Kummel, A. C.; Goodson, K. E. High Thermal Conductivity of Submicrometer Aluminum Nitride Thin Films Sputter-Deposited at Low Temperature. *ACS Nano* **2023**, 17 (21), 21240–21250. https://doi.org/10.1021/acsnano.3c05485.

(2) Chen, Y.; Wang, R.; Wang, B.; Xing, T.; Song, X.; Zhu, M.; Yan, H. Effects of Mean Free Path on the Preferentially Orientated Growth of AlN Thin Films. *J. Cryst. Growth* **2005**, 283 (3), 315–319. https://doi.org/10.1016/j.jcrysgro.2005.06.007.

(3) Iriarte G.F.; Rodríguez J.G.; Calle F. Synthesis of c-axis oriented AlN thin films on different substrates: A review. *Materials Research Bulletin* **2010**, 45 (9), 1039-1045. https://doi.org/10.1016/j.materresbull.2010.05.035.

(4) Patterson, A. L. The Scherrer Formula for X-Ray Particle Size Determination. *Phys Rev* **1939**, *56* (10), 978–982. https://doi.org/10.1103/PhysRev.56.978.

(5) Cahill, D. G. Thermal-Conductivity Measurement by Time-Domain Thermoreflectance. *MRS Bull.* **2018**, *43* (10), 782–789. https://doi.org/10.1557/mrs.2018.209.

(6) Kwon, H.; Perez, C.; Park, W.; Asheghi, M.; Goodson, K. E. Thermal Characterization of Metal–Oxide Interfaces Using Time-Domain Thermoreflectance with Nanograting Transducers. *ACS Applied Materials Interfaces* **2021**, 13, 58059–58065. https://doi.org/10.1021/acsami.1c12422

(7) Dames, C. Measuring the Thermal Conductivity of Thin Films : 3 Omega and Related Electrothermal Methods, Ch. 2. *Annu. Rev. Heat Transfer* **2013**, *16*, 7.

(8) Kodama, T.; Park, W.; Marconnet, A.; Lee, J.; Asheghi, M.; Goodson, K. E. In-Plane Thermal Conductivity Measurement on Nanoscale Conductive Materials with on-Substrate Device Configuration. In *13th InterSociety Conference on Thermal and Thermomechanical Phenomena in Electronic Systems*; **2012**; pp 250–255. https://doi.org/10.1109/ITHERM.2012.6231437.

(9) Xu, R. L.; Muñoz Rojo, M.; Islam, S. M.; Sood, A.; Vareskic, B.; Katre, A.; Mingo, N.; Goodson, K. E.; Xing, H. G.; Jena, D.; Pop, E. Thermal Conductivity of Crystalline AlN and the Influence of Atomic-Scale Defects. *J. Appl. Phys.* **2019**, *126* (18), 185105. https://doi.org/10.1063/1.5097172.

(10) Liu, W.; Balandin, A. A. Thermal Conduction in $Al_xGa_{1-x}N$ Alloys and Thin Films. *J. Appl. Phys.* **2005**, *97* (7), 073710. https://doi.org/10.1063/1.1868876.